

Enhanced Winter and Summer Trend Difference of MJO Intensity Since 1871

Ziyue Wang¹, Tim Li^{2,1}, Jianyun Gao³, and Melinda Peng⁴

1 Key Laboratory of Meteorological Disaster, Ministry of Education (KLME) / Joint International Research Laboratory of Climate and Environmental Change (ILCEC) / Collaborative Innovation Center on Forecast and Evaluation of Meteorological Disasters (CIC-FEMD), Nanjing University of Information Science and Technology, Nanjing, China

2 International Pacific Research Center and Department of Atmospheric Sciences, School of Ocean and Earth Science and Technology, University of Hawaii at Manoa, Honolulu, Hawaii 96822

3 Fujian Key Laboratory of Severe Weather, Fujian Meteorological Bureau, Fuzhou, Fujian, 350001, China

4 GD-IT/ Naval Research Lab., Monterey, California 93943

Submitted to *International Journal of Climatology*

This article has been accepted for publication and undergone full peer review but has not been through the copyediting, typesetting, pagination and proofreading process which may lead to differences between this version and the Version of Record. Please cite this article as doi: 10.1002/joc.6586.

Corresponding author: Tim Li, Department of Atmospheric Sciences, University of Hawaii at Manoa, Honolulu, Hawaii 96822. Email: timli@hawaii.edu

Abstract

Long-term winter and summer MJO trends in the past 138 years (1871 – 2008) were examined using National Oceanic and Atmospheric Administration (NOAA) 20th Century Reanalysis V2c dataset. It is found that MJO shows a distinctive different trend between boreal winter and summer. While the MJO intensity in both boreal winter and summer has a rising trend, the winter trend is much greater than the summer trend. As a result, the winter – summer difference shows a significant increasing trend. The distinctive winter and summer trends are attributed to the difference of atmospheric background circulation (such as vertical velocity) and static stability responses to the global warming between boreal winter and summer over equatorial eastern Indian Ocean. In boreal winter, both the surface moistening and strengthened ITCZ convection contribute to an increase of MJO activity. This is in contrast to boreal summer when a greater static stability and anomalous subsidence tend to offset the moistening effect, leading to a relatively weaker increase of the MJO activity.

Key words: Winter and summer MJO trend; global warming; RMM index

1. Introduction

The Madden-Julian Oscillation (MJO) is the most prominent intraseasonal mode in tropical atmosphere (Madden and Julian, 1994; Lau and Waliser, 2005; Zhang, 2005; Waliser, 2006) and the major predictability source for extended range forecast (Ferranti *et al.* 1990; Lau and Chang, 1992; Jones *et al.* 2000). MJO is characterized by a large-scale convective envelope with a dominant first-baroclinic vertical structure in free atmosphere, propagating eastward along the equator (Madden and Julian 1972; Wang *et al.* 2017, 2018; Wang and Li 2020). After initiated over tropical western Indian Ocean, MJO intensifies over the warm oceans (Zhao *et al.* 2013; Mei *et al.* 2015). The main convective activity associated with MJO is confined in the Indo-Pacific warm pool, but its upper-tropospheric circulation signal can propagate around the entire global tropics (Wang and Rui 1990, Li *et al.* 2015) and into higher latitudes (Ding and Wang 2007; Wang *et al.* 2013).

MJO exhibits significant seasonal variations in its intensity (Madden 1986), phase speed and direction of propagation (Wang and Rui 1990; Wu *et al.* 2005) and frequency (Hartmann *et al.* 1992). While boreal winter MJO is dominated by eastward propagation along the equator, boreal summer intraseasonal oscillation exhibits prominent northward propagation over tropical Indian Ocean and South China Sea (Yasunari, 1979, 1980; Gadgil and Srinivasan, 1990; Jiang *et al.* 2004) and northwestward propagation off the equatorial western North Pacific (Hartmann and Michelsen, 1989; Li and Wang 2005). The cause of the seasonality is possibly attributed to the meridional displacement of the thermal equator in boreal winter and summer over the Maritime Continent (Li 2014).

The trend of MJO intensity during recent decades has been examined. For example, Slingo *et al.* (1999) found that MJO appeared more active after 1976 than before. Zveryaev (2002) attributed the recently increased MJO activities over the

monsoon region to the increased local sea surface temperature (SST) over the tropical Indian Ocean. Jones and Carvalho (2006) noted that the enhanced MJO activity since 1976 includes both the increases of MJO amplitude and frequency. Tao *et al.* (2015) pointed out that during 1982-2009 the boreal summer ISO exhibited an increasing trend while the trend of the MJO in boreal winter was not significant.

All the aforementioned studies (e.g., Slingo *et al.* 1999; Zveryaev 2002; Jones and Carvalho 2006; Tao *et al.* 2015) were based on analysis of a relatively short period dataset, in which a trend was often mixed up with the change associated with natural interdecadal modes, such as the Interdecadal Pacific Oscillation (IPO) and the Atlantic Multi-decadal Mode (AMO). Thus, it is necessary to use a longer (greater than 100 years) dataset to separate the global warming and natural variability signals (Dai *et al.* 2015). Recently there were a number of studies about the future projection of MJO under global warming using CMIP5 (Coupled Model Intercomparison Project Phase 5) (e.g., Bui *et al.* 2018, 2019; Cui and Li 2019; Maloney *et al.* 2019; Rushley *et al.* 2019) or other models (e.g., Maloney and Xie 2013; Liu *et al.* 2013; Arnold *et al.* 2015; Chang *et al.* 2015). These studies showed that MJO would intensify in general (e.g., Rushley *et al.* 2019; Subramanian *et al.* 2014; Adames *et al.* 2017) and occur more frequently (Arnold *et al.* 2013; Chang *et al.* 2015). However, there is large uncertainty among these models, and most of these projections focused on the MJO intensity change in boreal winter. Motivated by these studies, we intend to use long-term observational and reanalysis data to isolate global warming signals from natural interdecadal modes to investigate the responses of MJO activities to increasing CO₂ in the past century, in a way similar to the future projection study with models. Furthermore, it has been shown that MJO exhibits a great seasonal difference in propagation (Wang and Rui 1990; Zhang *et al.* 2019), initiation (Jiang and Li 2005; Li *et al.* 2008; Zhao *et al.* 2013), and teleconnection patterns (Ding and Wang 2007). Few

of previous works examined the long-term trend difference between boreal winter and summer MJO. Given the distinctive summer and winter MJO behaviors, in this study we intend to separate winter and summer MJO trends.

The remaining part of this paper is organized as following. The data and methods are introduced in section 2. The winter and summer trends of MJO are presented in section 3. In section 4, we examine the physical mechanisms responsible for the winter and summer trend difference. Finally, a conclusion is given in section 5.

2. Data and Methods

2.1 Data

The main dataset used for this study is the NOAA 20th Century Reanalysis V2c (hereafter NOAA-20C) from 1871 to 2008 (Compo *et al.* 2011). Daily upper-level and lower-level zonal wind fields and upward outgoing longwave radiation flux at top of atmosphere (OLR) fields are used to measure the MJO intensity. It is worth mentioning that this reanalysis product assimilated only surface pressure, sea surface temperature and sea ice observations for the entire period, even though in the satellite era additional observations become available. The consistent use of the same data without incorporating new data sources guarantees no artificial jumps in the time series of variables, thereby casting confidence on the trend analysis. In addition, monthly mean sea surface temperature (SST) from the Hadley Center (Rayner *et al.* 2003) during 1871-2008 is used. The horizontal resolution of the SST data is $2^{\circ}\times 2^{\circ}$. The boreal winter (summer) is defined as the extended period from December to May (June to November).

To ensure that an MJO intensity index (described below) derived from the NOAA-20C is accurate in representing realistic MJO signals, a comparison is made first with the MJO index calculated using modern observations for a period of

1979-2008 (Cui *et al.* 2020). The observed daily OLR from NOAA (Liebmann and Smith 1996) and zonal wind fields from National Centers for Environmental Prediction-National Center for Atmospheric Research (NCEP-NCAR) Reanalysis I (Kalnay *et al.* 1996) are used for this purpose. The horizontal resolution is interpolated to $2.5^{\circ} \times 2.5^{\circ}$ for all datasets with 19 levels from 1000hPa to 100hPa.

2.2 Methods

The Real-time Multi-variate MJO (RMM) index developed by Wheeler and Hendon (2004) is computed to measure eastward-propagating MJO intensity and phase. The RMM indices using modern observations and those from NOAA-20C are computed for the same period (1979-2008) for comparison.

The following is the procedure to construct the RMM index. Firstly, all variables are subject to a 20-100-day filtering after removing a long-term linear trend, to remove the trend effect. Then the filtered wind and OLR fields are averaged over the tropical belt (15°S - 15°N). Next a multi-variable EOF analysis is performed, to obtain two leading EOF patterns and their associated normalized principal components ($PC1$ and $PC2$). As shown in Fig. 1, the two leading modes capture the major eastward-propagating MJO mode along the equator. The MJO intensity is approximately represented by the square root of the sum of square of two principal components ($\sqrt{PC1^2 + PC2^2}$).

The RMM index considers both the convection and circulation fields. To test the sensitivity of the trend analysis result to MJO definition, two additional MJO indices, with one considering only convection and the other only circulation, are also calculated. The calculation steps are similar to that of RMM. In the following, different notations are used to represent the different MJO indices mentioned above. RMM_NCEP represents the RMM index calculated based on 200hPa and 850hPa

zonal wind from NCEP/NCAR reanalysis I and satellite-measured OLR fields. RMM_NOAA denotes the RMM index calculated based on 200hPa and 850hPa zonal wind and OLR fields from NOAA-20C. RMM_OLR represents the convection-based RMM index with only OLR considered, and RMM_circulation represents the circulation-based RMM index calculated based on 200hPa and 850hPa zonal winds.

3. Winter and summer MJO trends

To examine whether or not the NOAA-20C is able to capture the MJO variability realistically, we first compare the two RMM indices, RMM_NCEP and RMM_NOAA, for the period of 1979-2008. Figure 1 shows the patterns of two leading EOF modes associated with the two RMM indices. In general, they bear similarity in the EOF patterns. For instance, the upper-level and lower-level zonal winds are opposite, indicating a first baroclinic mode vertical structure. Low-level easterlies (westerlies) appear to the east (west) of the MJO convection represented by a negative OLR center. From the lead-lagged correlation maps (Fig. 1 c-d), a significant negative correlation peak appears at day -10, indicating that EOF2 leads EOF1 by ten days, implying an eastward propagation.

As described in section 2, the overall MJO intensity can be defined as the square root of the sum of square of $PC1$ and $PC2$. To measure quantitatively how well the NOAA-20C is in reproducing the MJO intensity, we compute the correlation coefficients between the PC time series obtained from modern observations with NOAA-20C dataset for the period of 1979-2008, and the result is shown in Table 1. Note that the average correlation is around 0.8, exceeding a 99% confidence level. This adds confidence to use NOAA-20C to analyze the long-term trend of MJO intensity. The other two indices (considering either convection-only or circulation-only) also show high correlations with those calculated based on

RMM_NCEP. The results above are consistent with those of Kiladis (2014) and Li et al. (2015). While the index calculated based on the OLR-only was a little noisier compared to that calculated based on the circulation-only, these indices generally capture the MJO intensity and phase propagation characteristics.

Figure 2 shows the time series of the daily MJO intensity index derived from RMM_NOAA, which shows a marked increasing trend since 1871. To test whether this trend is statistically significant, the Mann-Kendall (MK) method (Kendall and Stuart, 1967; Mann, 1945) is used. The result indicates that the trend is statistically significant at a 99% confidence level. Figure 3 illustrates the winter and summer MJO trends. While both the winter and summer trends are statistically significant (exceeding a 99% confidence level), the winter trend is greater than the summer trend. Given that the climatologically winter MJO strength is greater than the summer MJO strength (Li and Hsu 2017), a much greater increase of the boreal winter MJO trend implies that the seasonal contrast of MJO variability increases in the past 138 years.

Figure 4a shows the time series of the winter and summer MJO intensity difference with RMM_NOAA. It shows an upward trend in the past 138 years. Our calculation of the P-value with the MK method indicates that the winter-summer difference has a significant positive trend at a 90% confidence level. It is worth noting that the distinctive trend differences are also evident and statistically significant with other MJO indices (Fig. 4b, 4c). Additionally, we conduct another analysis with different criteria for the strict season definition, that is, December-February (DJF) for winter and June-August (JJA) for summer. So-calculated winter-summer trend difference with RMM_NOAA is still statistically significant (not shown). This indicates that the seasonal contrast of MJO trend between boreal winter and summer is robust.

Fig. 5 directly shows the winter and summer MJO intensity trends, after the long-term annual mean trend is removed. Here, annual mean trend is the annual average of winter and summer trends. The MJO intensity in boreal winter and summer illustrates clear opposite trends, with a significant (exceeding a 90% confidence level) increasing (decreasing) trend in boreal winter (summer).

Another way to examine the trend difference between the winter and summer is to perform a skewness analysis. The skewness is a measure of the relative amplitude of positive and negative values of a time series. Following White (1980), the skewness is defined as

$$\text{Skewness} = m_3 / (m_2)^{3/2} ,$$

where m_k is the k th moment,

$$m_k = \sum_{i=1}^N \frac{(x_i - \bar{X})^k}{N} ,$$

x_i denotes the time series of winter and summer intensity difference at i th year, \bar{X} the long term mean of the time series, and N the number of years considered. The statistical significance of the skewness may be estimated such that a confidence level of 95% corresponds to the amplitude of the skewness exceeding ± 0.67 (Hong *et al.* 2008).

We calculated the skewness for different periods with RMM_NOAA. Table 2 lists the results. $N=30$ means that we compared the skewness values for the first and last 30 years. We tested the sensitivity of N from 30 to 60. Note that the skewness values are always significantly negative (positive) during the first (last) N years. This indicates that the difference between winter and summer MJO intensity is getting larger and larger.

To understand the connection between the winter and summer MJO trend and global SST evolution, we examine the time evolution of dominant global SST pattern during the past 138 years. An EOF analysis of 8-year low-pass filtered monthly global

SST field from 1871 to 2008 was conducted and the result is shown in Fig. 6. Before the EOF analysis, the long-term climatological annual cycle has been removed. The first leading EOF mode is a global warming pattern (Fig. 6a), whereas the second and third modes represent, respectively, the IPO and AMO modes (not shown). The correlation coefficients between the winter-summer trend difference and the time series of the three leading EOF modes are shown in Table 3. It is significantly correlated to the global warming time series, but not to the IPO or AMO mode. This implies that the winter-summer difference trend is caused by the global warming effect.

In the significance test above, the effective degree of freedom has been considered, following Davis (1976) and Chen (1982). Individual samples within a time series dataset after filtering may not be considered totally independent, which can be inferred from a higher auto correlation (Chen 1982; Davis 1976). This prompts the consideration of decrease of effective sample size when applied to t test, not simply equal to N (sample length)-2. The method used here for estimate of the new degree of freedom is simply based on the estimation of the cross-correlation. The effective degree of freedom is defined as $\frac{n}{T}$, with n being total number of sample data and

$$T = \sum_{\tau=-\infty}^{\infty} R_{xx}(\tau) \cdot R_{yy}(\tau) ,$$

where $R_{xx(yy)}(\tau)$ presents the auto correlation of variable $x(y)$, τ time lag. That is,

$$R_{xx}(\tau) = \frac{1}{n-\tau} \sum_{t=1}^{n-\tau} x_t^* \cdot x_{t+\tau}^*$$

$$R_{yy}(\tau) = \frac{1}{n-\tau} \sum_{t=1}^{n-\tau} y_t^* \cdot y_{t+\tau}^* .$$

τ is often set to the half of n and * means the standardized time series.

4. Physical cause of the winter-summer trend difference

To understand the mechanism responsible for the distinctive seasonal trend contrast, we examine the atmospheric and oceanic conditions associated with the MJO change. To better understand the winter-summer trend difference, the whole analysis period (1871-2008) is divided into Stage 1 (1871-1930), Transition period (1931-1948) and Stage 2 (1949-2008). The difference of background fields between Stage 2 and Stage 1 is examined to understand environmental controlling factors for the MJO as the MJO activities are much higher in Stage 2 than in Stage 1.

It has been shown that propagation features of boreal winter and summer intraseasonal oscillation modes are very different (e.g., Li and Wang 2005; Li 2014; Zhang and Li 2019). Given that the RMM index reflects primarily the eastward-propagating signal, it is desirable to select a common reference domain (10°S - 5°N , 75°E - 100°E), where MJO eastward propagation is most pronounced in both boreal winter and summer, for the subsequent diagnosis.

Figure 6 illustrates the dominant spatial patterns and time series of boreal winter (Fig. 6c, d) and summer (Fig. 6e, f) SST during the 138 year period. Given the similar explained variance, pattern and time series in boreal winter and summer (Fig. 6g, h), it is concluded that neither pattern nor time series of SST is a direct factor that causes the distinctive winter and summer trends of MJO intensity.

While the SST patterns look similar, the circulation fields are very different between Stage 2 and Stage 1. Figure 7 shows mid-tropospheric vertical velocity and lower-tropospheric moisture difference fields in boreal winter (right panel of Fig. 7). Accompanied with the difference fields are the long-term climatological fields in the same season (left panel, Fig. 7). The northern hemisphere winter climate in tropical Indo-Pacific warm pool is characterized by pronounced deep convection, mid-tropospheric ascending motion and low-level convergence along the

inter-tropical convergence zone (ITCZ) slightly south of the equator. The mean ascending motion and low-level convergence lead to high mean moisture in the equatorial Indian Ocean, where MJO variability is also high (Hsu and Li 2012a, Zhao *et al.* 2013). The difference fields show an overall increase in the ascending motion (Fig. 7b) and moisture (Fig. 7d), indicating a strengthened ITCZ over the eastern equatorial Indian Ocean, which favors the MJO development. As a result, both the amplitude and frequency of MJO may increase in Stage 2 compared to in Stage 1.

To sum up, the global warming leads to an increase of surface moisture and ascending motion in the key MJO variability region in boreal winter (Hsu and Li 2012b). Both factors favor the occurrence of more frequent (Arnold *et al.* 2013; Chang *et al.* 2015) and stronger (e.g., Subramanian *et al.* 2014; Adames *et al.* 2017; Rushley *et al.* 2019) MJOs. This leads to enhanced overall MJO variability (e.g., Liu *et al.* 2013; Maloney and Xie 2013; Maloney *et al.* 2019) in boreal winter.

In contrast, the background vertical velocity and moisture difference fields in boreal summer exhibit a distinctive feature. The background mean vertical velocity field in tropical Indian Ocean is characterized by two branches of ascending motion, one along the monsoon trough (15°N) and the other over the eastern equatorial Indian Ocean (Fig. 8a). Initiated over the equatorial Indian Ocean, MJO convective activity often propagates northward over Bay of Bengal in boreal summer (Jiang *et al.* 2004) while the dominant eastward propagation occurs in the equatorial eastern Indian Ocean (Jiang and Li 2005). In the mean state difference map, there is marked ascending motion along the monsoon trough, where the main convective zone in northern summer is located, but anomalous descending motion appears in the equatorial eastern Indian Ocean, Maritime Continent and equatorial western Pacific. Such anomalous descending motion tends to suppress MJO activity over the equatorial region, as demonstrated by a theoretical model of MJO (Li 2014).

In spite of descending motion induced surface divergence, the low-level moisture still increases near the equator (Fig. 8d), implying that the SST warming induced evaporation increase offsets the divergence effect. The overall increase of the moisture in the tropics favors the increase of MJO variance. This moisture effect is offset to a certain extent by the vertical velocity effect. As a result, a weaker increasing trend of MJO intensity is observed during the past 138 years.

To clearly demonstrate the cause of anomalous descending motion in the equatorial zone, we plotted the meridional – vertical structure of atmospheric overturning circulation averaged over 75°E-100°E (Fig. 9). Note that in boreal summer (Fig. 9b), the anomalous descending motion at the equatorial zone is closely related to enhanced convection over the monsoon trough. Therefore, it is likely that the global SST warming leads to a stronger Indian monsoon through “the richest get richer” mechanism (Hsu and Li 2012b), and the strengthened monsoon further induces anomalous subsidence over the equatorial region through the dynamic connection of local Hadley Cell. It is the anomalous subsidence that offsets the SST induced surface moistening effect and leads to a relatively weaker increase of MJO activity in northern summer. In contrast to boreal summer, the anomalous mid-tropospheric ascending motion occupies the entire tropical eastern Indian Ocean region in boreal winter.

Another factor to cause the winter and summer trend difference is the atmospheric static stability. The static stability was calculated at each vertical level, based on the following formula:

$$S = RT/C_p p - \partial T/\partial p,$$

where R denotes the gas constant, p the pressure, and C_p the specific heat at constant pressure. Figure 10 shows the difference of vertical profile of static stability averaged in reference region. A greater background static stability difference field appears in

boreal summer than in boreal winter. This implies that global warming induced static stability increase is greater in boreal summer than winter. As a result, MJO variability is suppressed more in boreal summer than in boreal winter. This favors greater MJO variability in boreal winter under global warming.

5. Conclusion

The long-term trend of MJO intensity is examined using NOAA 20th Century Reanalysis dataset for a centennial period from 1871 to 2008. A multi-variate MJO index with the 20-100-day filtered 200hPa and 850hPa zonal wind and OLR fields is used to define the MJO intensity. It is found that the amplitude of MJO intensity increases significantly during the past 138 years. A further separation of boreal winter and summer MJO variability indicates that the winter increasing trend is greater than the summer trend, implying an enhanced winter-summer difference in MJO activity since 1871 with use of three different RMM indices.

To quantitatively and clearly demonstrate key process and compare the seasonal difference, we show the difference of low-level specific humidity (averaged for 1000-700hPa), mid-tropospheric vertical p-velocity (averaged at 500-300hPa) and column mean static stability (100hPa-300hPa) between Stage 2 and Stage 1 averaged over the key reference region in boreal winter and summer (Fig. 11). The cause of the distinctive winter and summer trends is primarily attributed to the difference in the vertical velocity trend in the eastern equatorial Indian Ocean associated with the vertical-meridional overturning circulation in the region. In boreal winter, global SST warming causes enhanced convection and ascending motion over the oceanic ITCZ over tropical Indian Ocean and along South Pacific Convergence zone (SPCZ). This vertical velocity effect works together with the increased surface moisture in place causes the strengthened MJO variability in northern winter. In boreal summer,

climatologically there are two zonally oriented convective zones over the tropical Indian Ocean. One is along the monsoon trough and the other is near the equator. Anomalous convection along the two zones often exhibits a seesaw characteristic, with enhanced convection in one zone but suppressed convection in the other (Jiang *et al.* 2004; Qi *et al.* 2008). In response to global warming, the monsoon precipitation is enhanced, and the enhanced monsoon convection induces anomalous Hadley circulation and thus anomalous subsidence over the equatorial zone (Hsu and Li 2012b). The suppressed convection in the equatorial region tends to weaken the eastward-propagating MJO mode, offsetting the moisture effect. As a result, a relatively weaker increasing trend of eastward-propagating MJO is observed for the boreal summer. Thus, the cause of the distinctive seasonal contrast lies on background mean vertical velocity change under global warming. In addition, a greater increase of atmospheric static stability in boreal summer under global warming also helps strengthen the winter–summer MJO trend difference.

Most of previous studies on MJO future projection under global warming focused on MJO intensity change during boreal winter (e.g., Liu *et al.* 2013; Arnold *et al.* 2015; Maloney 2019; Cui and Li 2019). They concluded that MJO intensity would strengthen under global warming, which is consistent with the current result that the winter MJO intensity increases during the past 138 years. On the other hand, Jones and Carvalho (2006) pointed out that a positive linear trend of MJO intensity was observed since 1960s in both the summer and winter seasons, and the boreal summer trend appeared greater. Tao *et al.* (2015) also found a stronger positive trend in boreal summer with a shorter period. Such a seasonal contrast differs from the current analysis. This points out that the trend is sensitive to the period studied. Jones and Carvalho (2006) and Tao *et al.* (2015) used a data period shorter than 50 years. As a result, their results are greatly influenced by natural interdecadal fluctuations. A

longer period is needed to separate the global warming signal from the interdecadal signal. Indeed, data quality in earlier 20th century is not as good as in later periods. But this is what we have. Model data have even more serious biases.

In this study we focused on the analysis of long-term reanalysis data. It would be interesting to further examine the winter and summer MJO trends in various CMIP5 models under different global warming scenarios. How the change of background circulation (such as anomalous ascending or descending motion) and moisture fields affects MJO intensity and frequency is another open issue, which requires further investigation with idealized numerical model experiments. These issues will be addressed in future endeavor.

Acknowledgements. This work was jointly supported by China National Key R&D Program 2017YFA0603802 and 2018YFC1505805, NSFC grants 41875069 and 41575043, NOAA NA18OAR4310298, and NSF AGS-1643297. This is SOEST contribution number 12345, IPRC contribution number 1234 and ESMC number 123.

References

- Adames, Á. F., D. Kim, A. H. Sobel, A. D. Genio, and J. Wu, 2017: Changes in the structure and propagation of the MJO with increasing CO₂. *J. Adv. Model. Earth Syst.*, **9**, 1251–1268, <https://doi.org/10.1002/2017MS000913>.
- Arnold, N. P., Z. Kuang, and E. Tziperman, 2013: Enhanced MJO-like variability at high SST. *J. Climate*, **26**, 988–1001, <https://doi.org/10.1175/JCLI-D-12-00272.1>
- Arnold, N.P., M. Branson, Z. Kuang, D.A. Randall, and E. Tziperman, 2015: MJO Intensification with Warming in the Superparameterized CESM. *J. Climate*, **28**, 2706–2724.
- Bui, H. X., and E. D. Maloney, 2018: Changes in Madden-Julian Oscillation precipitation and wind variance under global warming. *Geophys. Res. Lett.*, **45**, 7148–7155.
- Bui, H. X., and E. D. Maloney, 2019: Mechanisms for global warming impacts on Madden-Julian Oscillation precipitation amplitude. *J. Climate*, **32**, 6961–6975.
- Chang, C.-W. J., W.-L. Tseng, H.-H. Hsu, N. Keenlyside, and B.-J. Tsuang, 2015: The Madden-Julian oscillation in a warmer world. *Geophys. Res. Lett.*, **42**, 6034–6042, <https://doi.org/10.1002/2015GL065095>.
- Chen W. Y. 1982. Fluctuation in northern hemisphere 700-mb height field associated with the Southern Oscillation. *Mon Weather Rev.*, **110**: 808–823
- Compo, G., and Coauthors. 2011. The twentieth century reanalysis project. *Quart. J. Roy. Meteor. Soc.*, **137**, 1–25.
- Cui, J., and Li, T. 2019. Changes of MJO propagation characteristics under global warming. *Clim Dyn.*, **53**: 5311. <https://doi.org/10.1007/s00382-019-04864-4>
- Cui, J., L. Wang, T. Li, B. Wu, 2020: Can reanalysis products with only surface variables assimilated capture Madden–Julian oscillation characteristics? *International Journal of Climatology*, **40**(2), 1279–1293.

- Dai, A., J. Fyfe, S.-P. Xie, X. Dai. 2015. Decadal modulation of global surface temperature by internal climate variability. *Nature Climate Change*, **5**, 555–559.
- Davis, R. E., 1976: Predictability of sea surface temperature and sea level pressure anomalies over the North Pacific Ocean. *J. Phys. Oceanogr.*, **6**, 249–266, doi: 10.1175/1520-0485(1976)006<0249:POSSTA>2.0.CO;2
- Ding, Q., and B. Wang. 2007. Intraseasonal interaction between the Eurasian wave train and the Indian summer monsoon. *J. Climate*, **20**, 3751–3767.
- Ferranti, L., Palmer, T. N., Molteni F, and Klinker K. 1990. Tropical-extratropical interaction associated with the 30-60 day oscillation and its impact on medium and extended range prediction. *J Atmos Sci.*, **47**, 2177-2199
- Gadgil, S., and J. Srinivasan. 1990. Low frequency variation of tropical convergence zones. *Meteor. Atmos. Phys.*, **44**(1–4), 119–132.
- Hartmann, D. L., and Michelsen, M. L. 1989. Intraseasonal periodicities in Indian rainfall. *J. Atmos. Sci.*, **46**(18), 2838-2862.
- Hartmann, D. L., M. L. Michelsen, and S. A. Kelein. 1992. Seasonal variations of tropical intraseasonal oscillations: A 20–25-day oscillation in the western Pacific. *J. Atmos. Sci.*, **49**(14), 1277–1289.
- Hong, C., T. Li, LinHo, and J. Kug. 2008: Asymmetry of the Indian Ocean Dipole. Part I: Observational Analysis. *J. Climate*, **21**, 4834–4848.
- Hsu, P.-C., and T. Li. 2012a. Role of the boundary layer moisture asymmetry in causing the eastward propagation of the Madden-Julian Oscillation. *J. Climate*, **25**(14), 4914-4931.
- Hsu, P.-C., and T. Li. 2012b. Is “rich-get-richer” valid for Indian Ocean and Atlantic ITCZ?, *Geophys. Res. Lett.*, **39**, L13705.

- Jiang, X. N., T. Li, and B. Wang. 2004. Structures and Mechanisms of the Northward Propagating Boreal Summer Intraseasonal Oscillation. *Journal of Climate*. **17**(5): 1022–1039.
- Jiang, X., and T. Li, 2005: Re-initiation of the boreal summer intraseasonal oscillation in the tropical Indian Ocean. *J. Climate*, **18**, 3777-3795.
- Jones, C., and Carvalho LMV. 2006. Changes in the activity of the Madden–Julian Oscillation during 1958–2004. *J. Clim.* **19**: 6353–6370.
- Jones, C., Waliser, D., Schemm, JK. *et al.* 2000. Prediction skill of the Madden and Julian Oscillation in dynamical extended range forecasts. *Clim. Dyn.*, **16**: 273. <https://doi.org/10.1007/s003820050327>
- Kalnay *et al.* 1996. The NCEP/NCAR 40-year reanalysis project. *Bull. Amer. Meteor. Soc.*, **77**: 437-470
- Kendall, M. A., and Stuart, A. 1967. *The Advanced Theory of Statistics*, (2nd ed.). Londres: Charles Griffin
- Kiladis G N , Dias J , Straub K H , et al. 2014. A Comparison of OLR and Circulation-Based Indices for Tracking the MJO. *Mon. Wea. Rev.*, **142**(5):1697-1715.
- Lau, K. M., Chang, F. C. 1992. Tropical intraseasonal oscillation and its prediction by the NMC operational model. *J. Clim.*, **5**: 1365-1378
- Lau, K. M., and D. E. Waliser, 2005. Intraseasonal variability of the Atmosphere-Ocean Climate System. *Springer*, Heidelberg, Germany, 474 pp.
- Li, T. 2014. Recent Advance in Understanding the Dynamics of the Madden-Julian Oscillation, *J. Meteor. Res.*, **28**, 1-33.
- Li, T., C. Zhao, P.-C. Hsu, and T. Nasuno. 2015. MJO Initiation Processes over the Tropical Indian Ocean during DYNAMO/CINDY2011. *J. Climate*, **28**, 2121-2135.

- Li, T., F. Tam, X. Fu, T. Zhou, and W. Zhu, 2008: Causes of the Intraseasonal SST Variability in the Tropical Indian Ocean, *Atmosphere-Ocean Science Letters*, **1**, 18-23.
- Li, T., and B. Wang. 2005. A review on the western North Pacific monsoon: synoptic-to-interannual variabilities. *Terrestrial, Atmospheric and Oceanic Sciences*, **16**, 285-314.
- Li, T., and P.-C. Hsu. 2017. Fundamentals of Tropical Climate Dynamics, *Springer*, ISBN 978-3-319-59595-5.
- Liebmann, B., and C. A. Smith, 1996: Description of a complete (interpolated) outgoing longwave radiation dataset. *Bull. Amer. Meteor. Soc.*, **77**, 1275–1277.
- Liu P, Li T, Wang B, Zhang MH, Luo JJ *et al.* 2013: MJO change with A1B global warming estimated by the 40-km ECHAM5. *Clim Dyn.*, **41**:1009–1023
- Madden, R. A., and P. R. Julian. 1972. Description of global-scale circulation cells in the tropics with a 40–50-day period. *Atmos. Sci.*, **29**(6): 3138–3158.
- Madden, R. A. 1986. Seasonal variations of the 40-50-day oscillation in the tropics. *J. Atmos. Sci.*, **43**(24), 3138-3158.
- Madden, R. A., and P. R. Julian. 1994. Observational of 40-50-day tropical oscillation–A review. *Mon. Wea. Rev.*, **122**(5), 814-837
- Maharaj E, Wheeler M (2005) Forecasting an index of the Madden–Julian Oscillation. *Int J Climatol* 25:1611–1618
- Maloney, E. D., Adames, Á. F. and Bui, H. X. 2019. Madden–Julian oscillation changes under anthropogenic warming. *Nature Clim Change* **9**, 26–33.
- Maloney, E. D., and S.-P. Xie, 2013: Sensitivity of tropical intraseasonal variability to the pattern of climate warming. *J. Adv. Model. Earth Syst.*, **5**, 32–47, <https://doi.org/10.1029/2012MS000171>.

- Mann, H. B. 1945. Non-parametric tests against trend. *Econometrica*, **13**(3), 245–259.
<https://doi.org/10.2307/1907187>
- Mei, S., T. Li, and W, Chen. 2015. Three types of MJO Initiation Processes over Western Equatorial Indian Ocean. *Advances in Atmospheric Sciences*, **32**(9): 1208-1216
- Qi, Y., R. Zhang, T. Li, and M. Wen. 2008. Interactions between the summer mean monsoon and the intraseasonal oscillation in the Indian monsoon region, *Geophys. Res. Lett.*, **35**, L17704, doi:10.1029/2008GL034517.
- Rayner, N. A., D. E. Parker, E. B. Horton, C. K. Folland, L. V. Alexander, D. P. Rowell, E. C. Kent, and A. Kaplan. 2003. Global analyses of sea surface temperature, sea ice, and night marine air temperature since the late nineteenth century. *J. Geophys. Res.*, **108**(D14), 4407, doi:10.1029/2002JD002670.
- Rushley, S.S., D. Kim, and Á.F. Adames, 2019: Changes in the MJO under Greenhouse Gas–Induced Warming in CMIP5 Models. *J. Climate.*, **32**, 803–821, <https://doi.org/10.1175/JCLI-D-18-0437.1>
- Slingo JM, Powell DP, Sperber KR, and Nortley F. 1999. On the predictability of the interannual behavior of the Madden-Julian oscillation and its relationship with El Nino. *Q J R Meteorol Soc*, **125**, 583-609
- Subramanian, A., M. Jochum, A. J. Miller, R. Neale, H. Seo, D. Waliser, and R. Murtugudde, 2014: The MJO and global warming: A study in CCSM4. *Climate Dyn.*, **42**, 2019–2031, <https://doi.org/10.1007/s00382-013-1846-1>.
- Tao, L., J. W. Zhao., and T. Li. 2015. Trend analysis of tropical intraseasonal oscillations in the summer and winter during 1982–2009. *Int. J. Climatol.* **35**: 3969–3978
- Waliser D.E. 2006. Intraseasonal Variability. In: Wang B (ed) *The Asian monsoon*. Springer, Heidelberg, pp 203–258

- Accepted Article
- Wang, B., and H. Rui. 1990. Synoptic climatology of transient tropical intraseasonal convection anomalies, 1975– 1985. *Meteor. Atmos. Phys.*, **44**(1–4), 43–61.
- Wang L, Li T, 2020: Effect of vertical moist static energy advection on MJO eastward propagation: sensitivity to analysis domain. *Climate Dynamics* 54:2029–2039.
- Wang, L., T. Li, and T. Nasuno, 2018: Impact of Rossby and Kelvin Wave Components on MJO Eastward Propagation. *Journal of Climate*, 31 (17), 6913-6931.
- Wang, L., T. Li, E. Maloney, B. Wang, 2017: Fundamental Causes of Propagating and Non-propagating MJOs in MJOTF/GASS models. *Journal of Climate*, 30 (10), 3743-3769.
- Wang, L., T. Li, T. Zhou and X. Rong, 2013: Origin of the Intraseasonal Variability over the North Pacific in Boreal Summer. *Journal of Climate*, 26(4), 1211-1229.
- White, H. G. 1980. Skewness, kurtosis and extreme values of Northern Hemisphere geopotential heights. *Mon. Wea. Rev.*, **108**, 1446–1455.
- Wheeler, M. C., and H. H. Hendon. 2004. An All-Season Real-Time Multivariate MJO Index: Development of an Index for Monitoring and Prediction. *Monthly Weather Review*. **132**(8): 1979-1932
- Wu, M. L. C., S. D. Schubert, M. J. Suarez, *et al.* 2005. Seasonality and meridional propagation of the MJO. *J. Climate*, **19**(10), 1901–1921.
- Yasunari, T. 1979. Cloudiness fluctuation associated with the Northern Hemisphere summer monsoon. *J. Meteor. Soc. Japan*, **57**, 227–242.
- Yasunari, T. 1980. A quasi-stationary appearance of 30–40 day period in the cloudiness fluctuation during summer monsoon over India. *J. Meteor. Soc. Japan*, **58**, 225–229.
- Zhao, C., T. Li, and Zhou, T. 2013. Precursor Signals and Processes Associated with MJO Initiation over the Tropical Indian Ocean. *J. Climate*, **26**(1): 291–307.

- Zhang, C. 2005. Madden-Julian oscillation. *Rev. Geophys.* **43**, RG2003, doi: 10.1029/2004RG000158
- Zhang, Q. C., T. Li, and J. Liu, 2019: Contrast of evolution characteristics of boreal summer and winter intraseasonal oscillations over tropical Indian Ocean. *J. Meteor. Res.*, 33(4), 678–694, doi: 10.1007/s13351019-9015-z.
- Zveryaev II. 2002. Interdecadal changes in the zonal wind and the intensity of intraseasonal oscillations during boreal summer Asian monsoon. *Tellus*, **54A**: 288–298.

Figure Captions

Fig. 1 (Top and middle panel) Leading EOF patterns of 850hPa zonal wind (red line), 200hPa zonal wind (blue line) and OLR (black line) associated with (a) RMM_NCEP, (b) RMM_NOAA and for the period of 1979-2008. (Bottom panel) Lead-lag correlations between two leading EOFs (c-d). The red line in (c, d) represents the threshold of 95% significant correlation.

Fig. 2 Time series of the MJO intensity index associated with RMM_NOAA from 1871-2008 (black line). Blue curve represents a 91-day running mean. Red curve represents the long-term trend, exceeding a 99% confidence level with Mann-Kendall test.

Fig. 3 Time series of the boreal winter (blue) and summer (red) MJO intensity index associated with RMM_NOAA from 1871-2008. The trend of winter (summer) is 0.055 (0.040) per decade. Both the trends exceed a 99% confidence level with Mann-Kendall test.

Fig. 4 Time series (bar) of the MJO winter (December-May) and summer (June-November) difference index (winter minus summer) from (a) RMM_NOAA, (b) RMM_circulation and (c) RMM_OLR since 1871. Black line represents the trend of winter-summer difference. All trends exceed a 90% confidence level with Mann-Kendall test.

Fig. 5 Time series of boreal winter (blue line) and summer (red line) MJO intensity indices (minus annual mean trend) and their trends associated with RMM_NOAA. Both the winter and summer trends exceed a 90% confidence level with Mann-Kendall test.

Fig. 6 The first EOF mode patterns (left) and corresponding time series (right) of global monthly 8-year low-pass filtered SST fields in all seasons (a, b), boreal

winter only (c, d) and boreal summer only (e, f) for the period of 1871-2008. The difference between boreal winter and summer is shown in bottom panel.

Fig. 7 Climatological mean vertical p-velocity field (a, Pa/s, averaged at 500-300hPa) and specific humidity field (c, kg/kg, averaged at 1000-700hPa) in boreal winter during 1871-2008 and the difference fields of the mean vertical velocity (b) and specific humidity (d) between Stage 2 and Stage 1. The rectangle indicates the key analysis region. Stippling denotes 99% confidence level according to the Student's *t* test.

Fig. 8 As in Fig. 7, except for boreal summer.

Fig. 9 Meridional-vertical cross section of the vertical overturning circulation (streamline; $\omega \cdot 1000$) and vertical p-velocity (ω , shaded, Pa/s) difference fields between Stage 2 and Stage 1 averaged over 75°E-100°E in boreal (a) winter and (b) summer.

Fig. 10 Difference of vertical profile of atmospheric static stability (winter: dash; summer: solid) between Stage 2 and Stage 1 averaged over (10°S-5°N, 75°E-100°E).

Fig. 11 The difference of background specific humidity (10^{-4} kg/kg, 1000-700hPa), vertical p-velocity (10^{-3} Pa/s, 500-300hPa) and static stability (10^{-6} , 1000-300hPa) between Stage 2 and Stage 1 averaged over (10°S-5°N, 75°E-100°E) in boreal winter (blue) and summer (orange).

Table captions

Table 1: Correlation coefficients between the time series (1979-2008) of PC1, PC2 and the MJO intensity index derived from RMM_NCEP index and those from the 20th Century Reanalysis product for a combined circulation-OLR index (RMM_NOAA), a circulation-only index (RMM_circulation) and a OLR-only index (RMM_OLR). The values that exceed the 99% confidence level are marked in bold (by an asterisk).

Table 2: The skewness of winter-summer difference time series during the first and last N year periods. The values that exceed the 95% confidence level (set to ± 0.67) are marked in bold (by an asterisk).

Table 3: Correlation coefficients between winter-summer difference and global warming, IPO, AMO time series. The values that exceed the 90% confidence level are marked in bold (by an asterisk). The value in bracket represents the degree of freedom, based on the method used in Chen (1982).

Table 1: Correlation coefficients between the time series (1979-2008) of PC1, PC2 and the MJO intensity index derived from RMM_NCEP index and those from the 20th Century Reanalysis product for a combined circulation-OLR index (RMM_NOAA), a circulation-only index (RMM_circulation) and a OLR-only index (RMM_OLR). The values that exceed the 99% confidence level are marked in bold (by an asterisk).

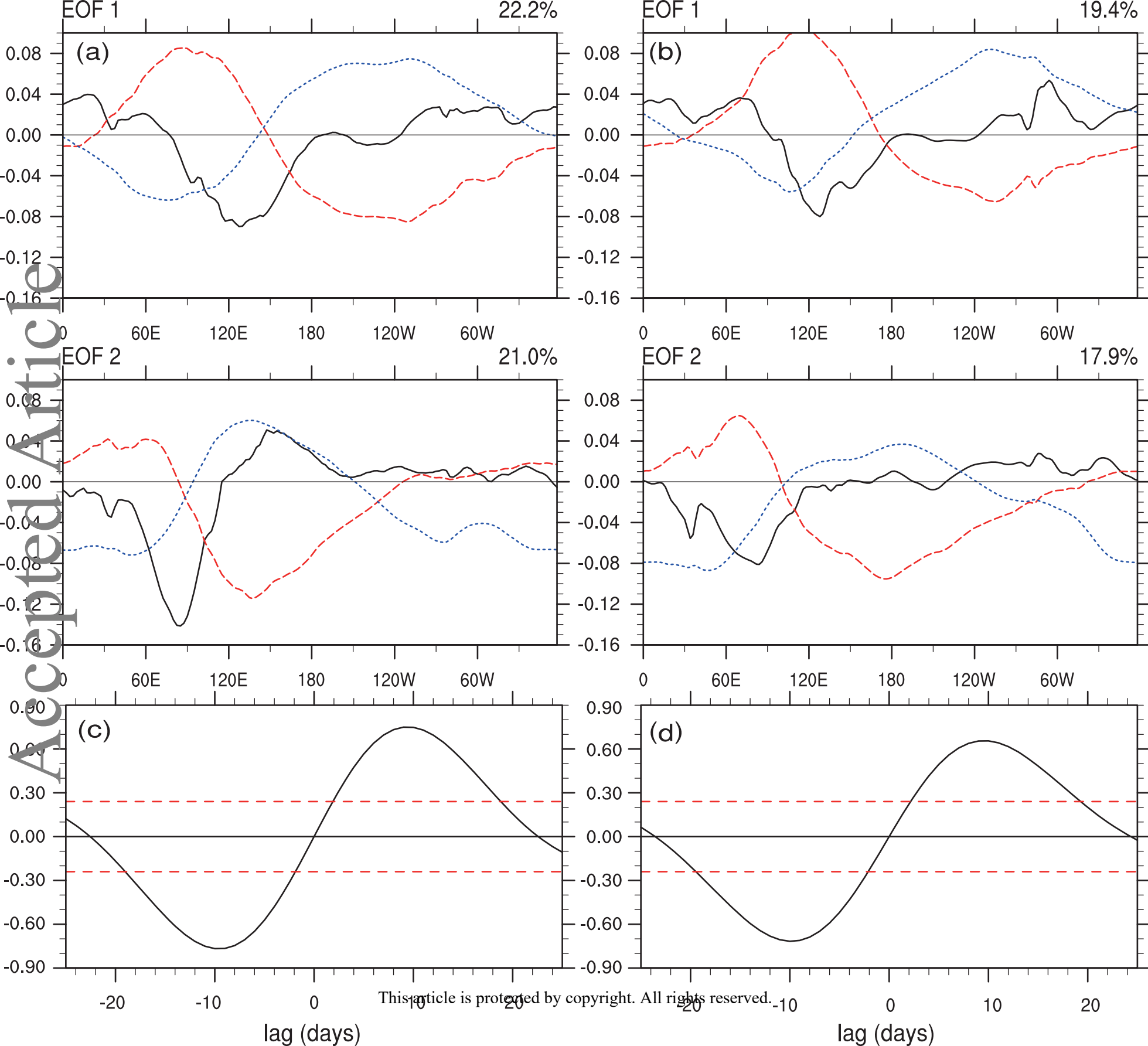
	PC1	PC2	MJO Index
RMM_NOAA	0.75*	0.74*	0.88*
RMM_circulation	0.83*	0.79*	0.84*
RMM_OLR	0.67*	0.44*	0.42*

Table 2: The skewness of winter-summer difference time series during the first and last N year periods. The values that exceed the 95% confidence level (set to ± 0.67) are marked in bold (by an asterisk).

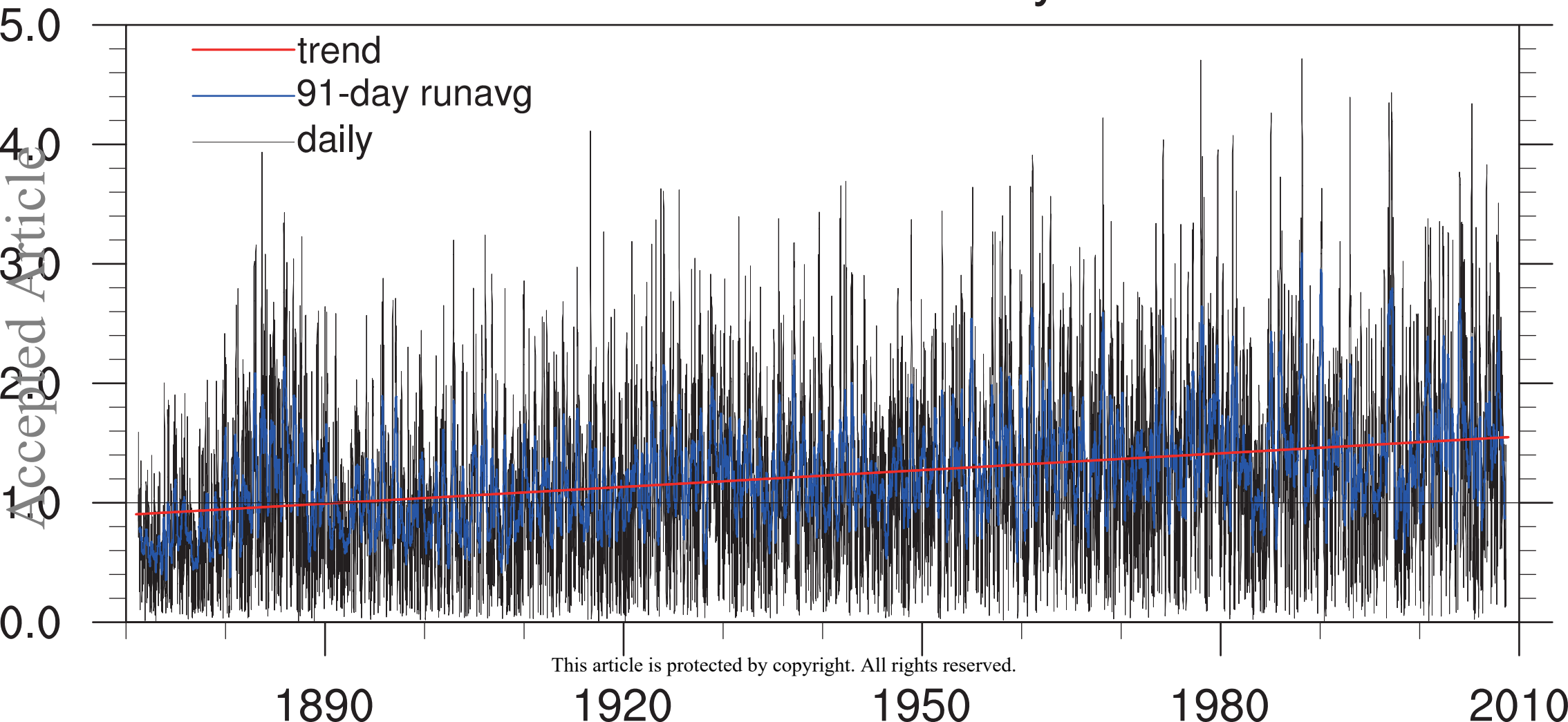
	First N years	Last N years
N=30	-1.25*	1.08*
N=40	-1.04*	1.0*
N=50	-0.93*	1.08*
N=60	-1.13*	1.13*

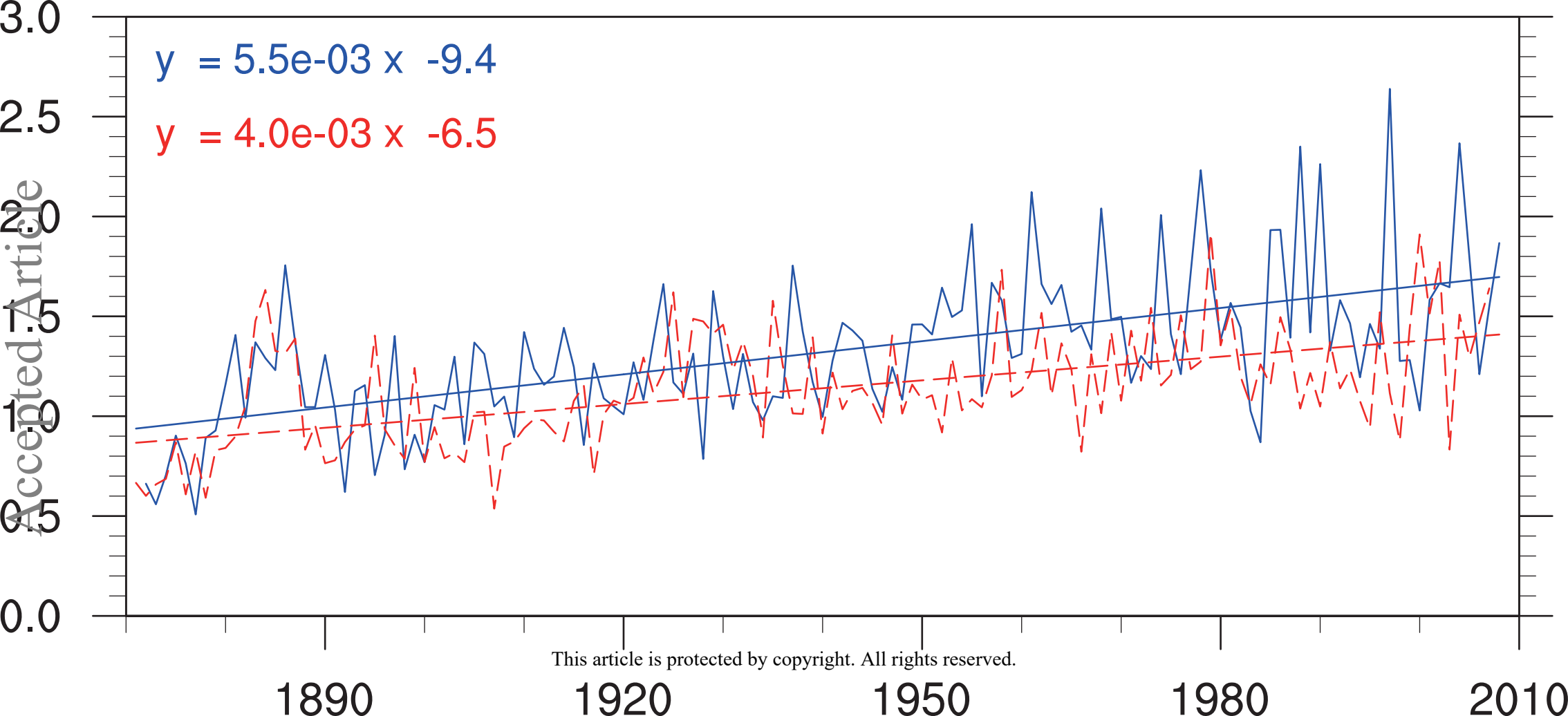
Table 3: Correlation coefficients between winter-summer difference and global warming, IPO, AMO time series. The values that exceed the 90% confidence level are marked in bold (by an asterisk). The value in bracket represents the degree of freedom, based on the method used in Chen (1982).

	Global Warming	IPO	AMO
Dif_NOAA	0.18(91)*	-0.01(122)	-0.09(109)

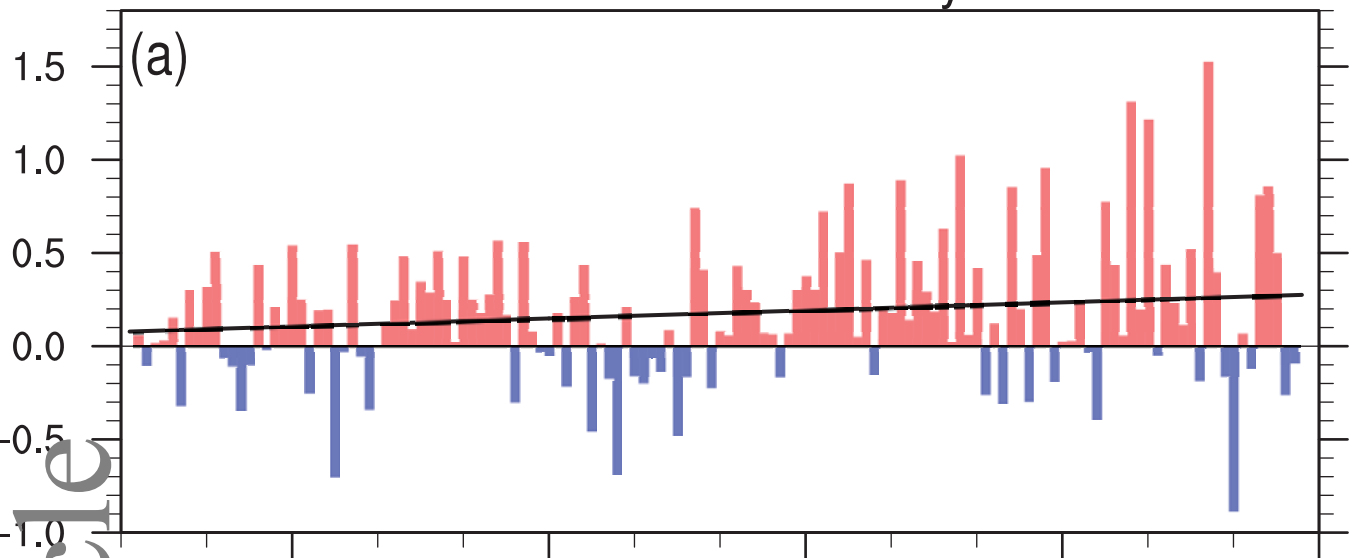


$$y = 5.3e-07 x + 0.6$$

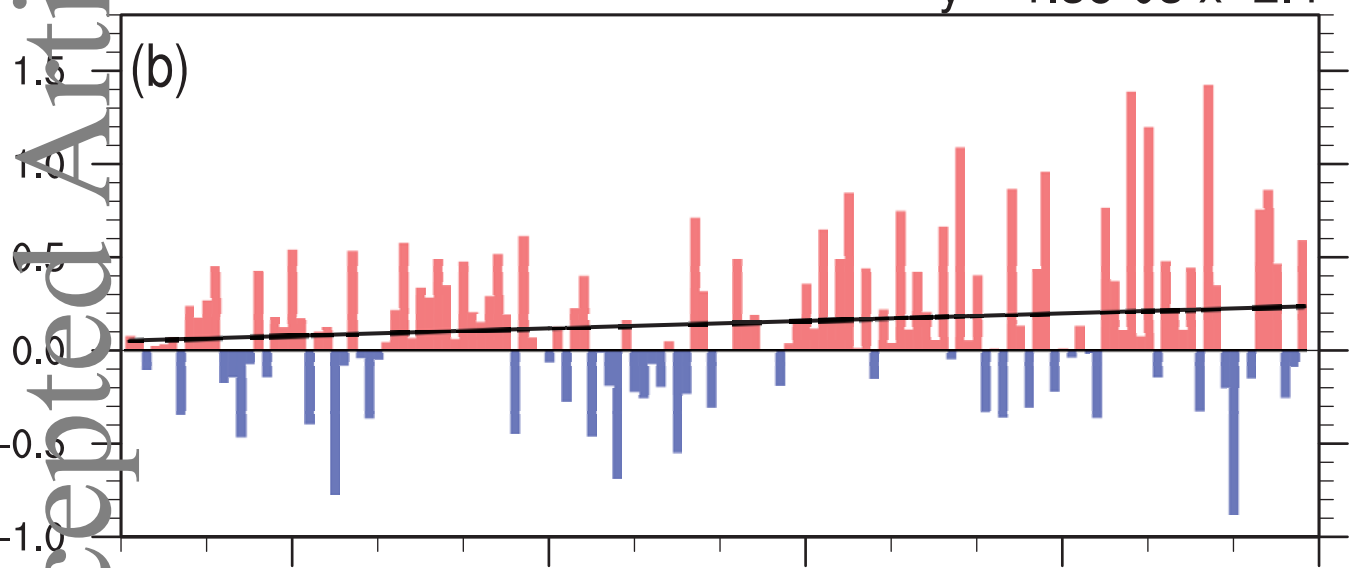




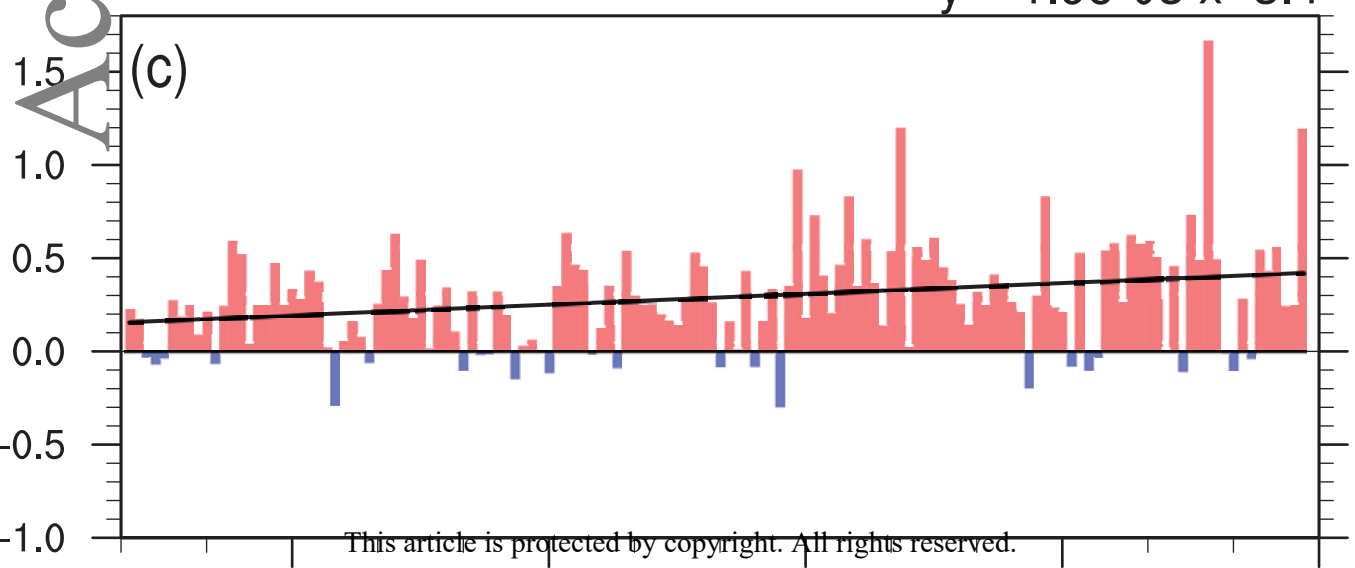
$$y = 1.4e-03 x - 2.6$$



$$y = 1.3e-03 x - 2.4$$



$$y = 1.9e-03 x - 3.4$$



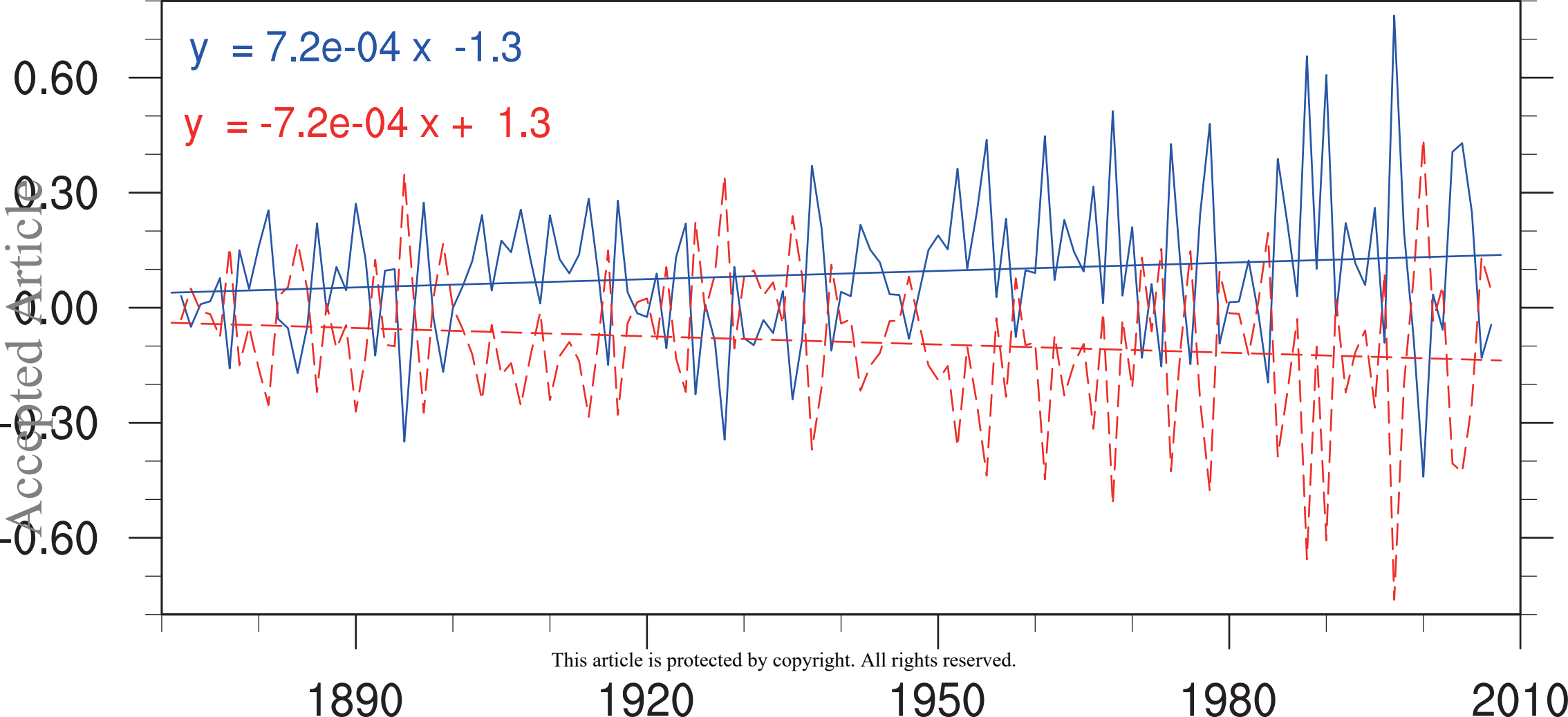
1890

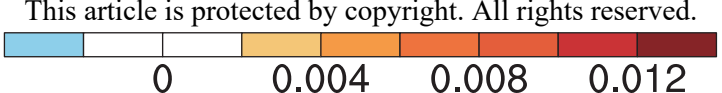
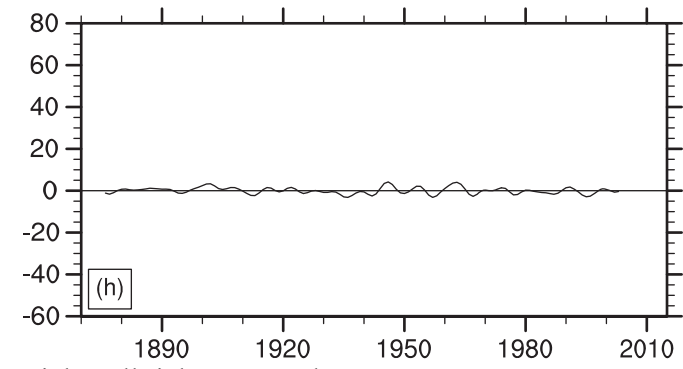
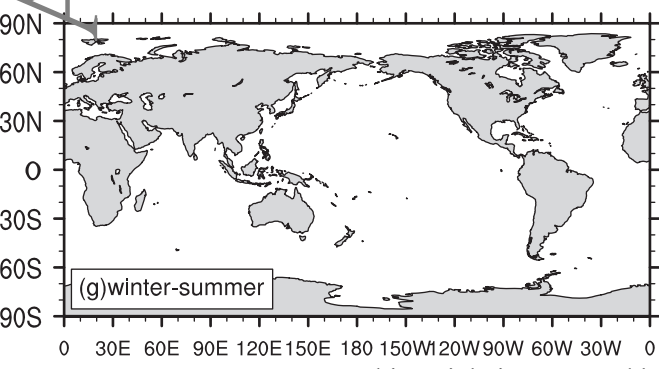
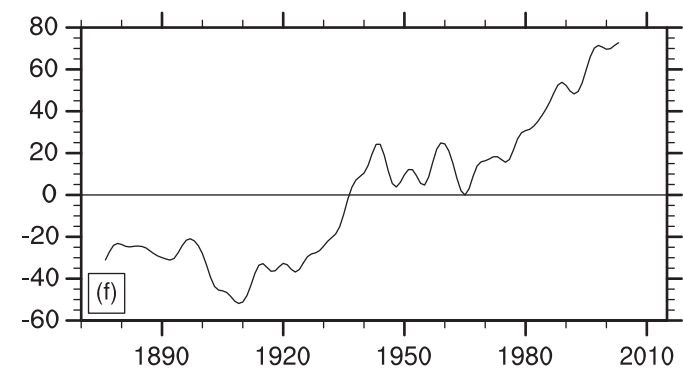
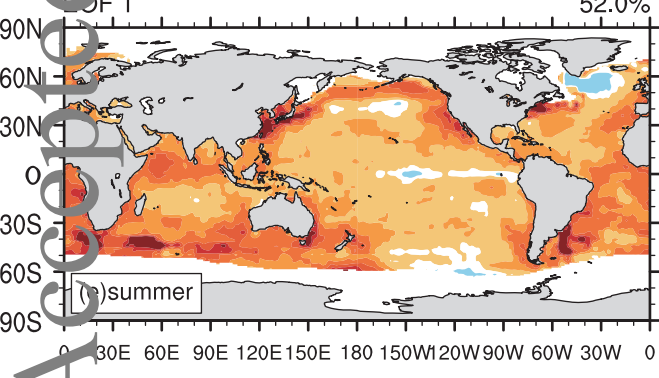
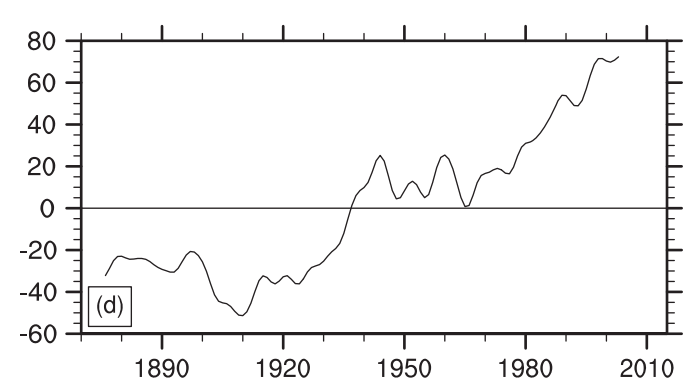
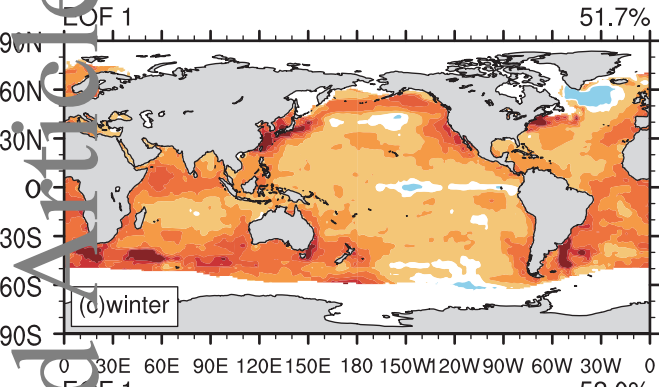
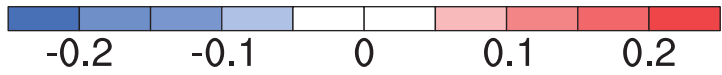
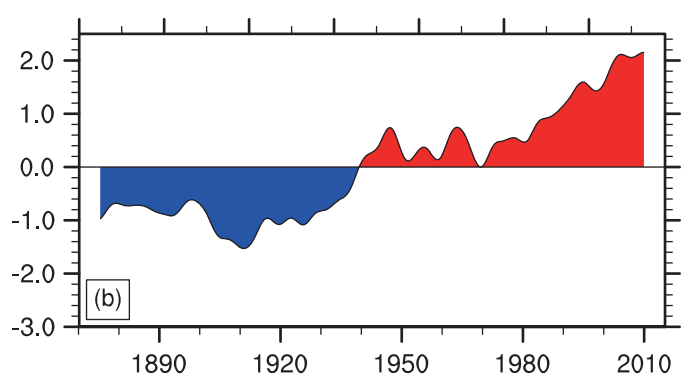
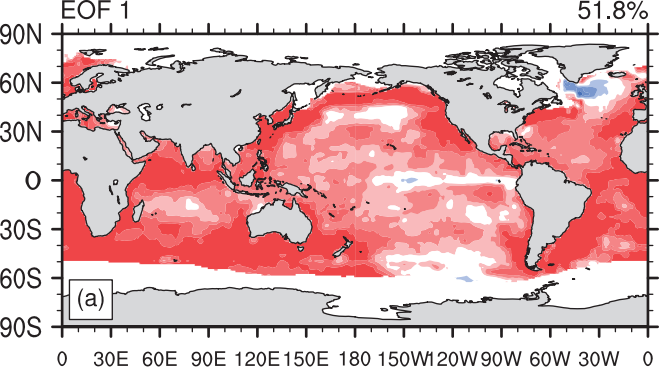
1920

1950

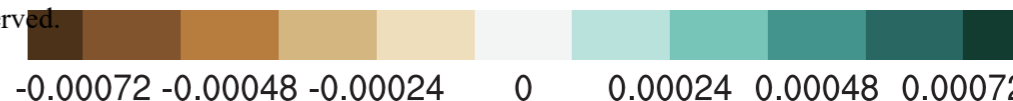
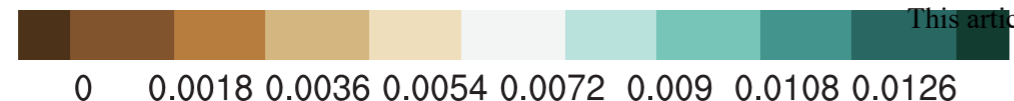
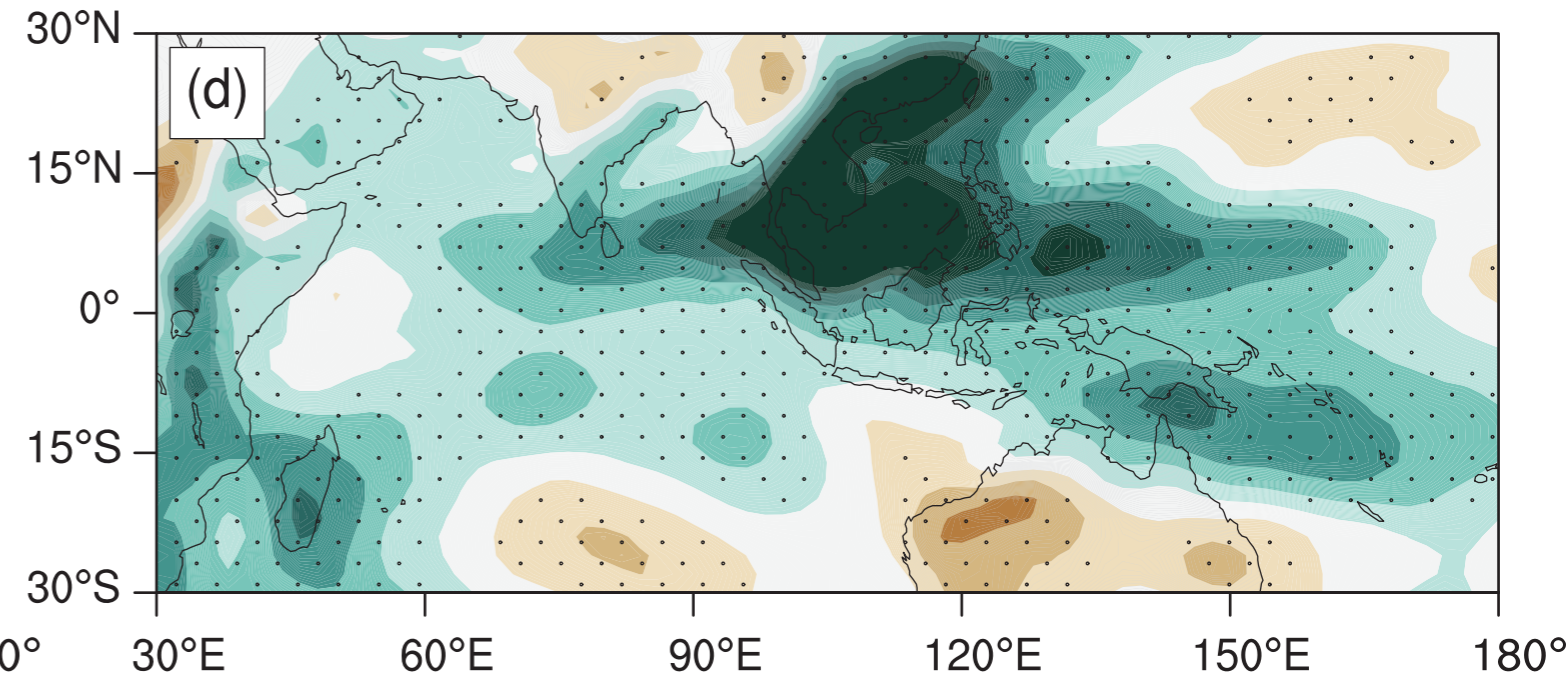
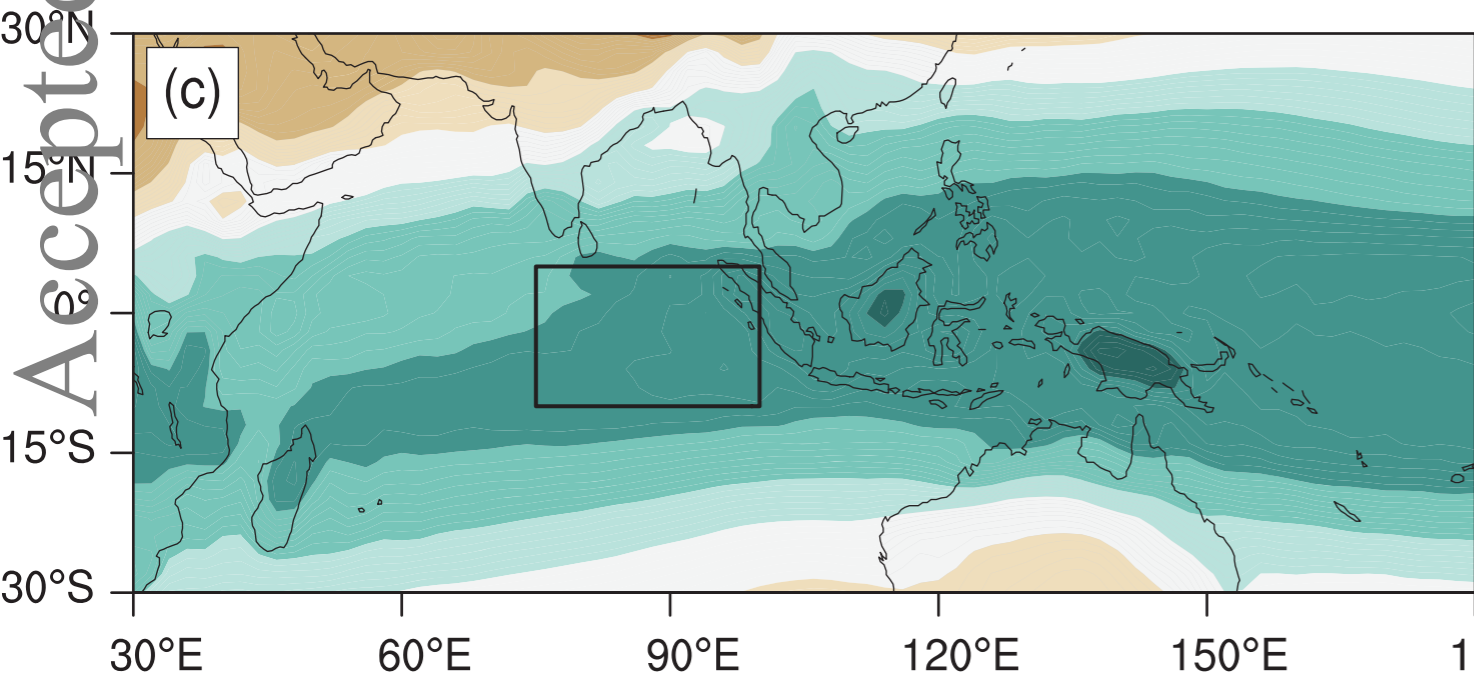
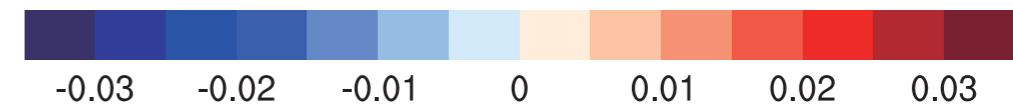
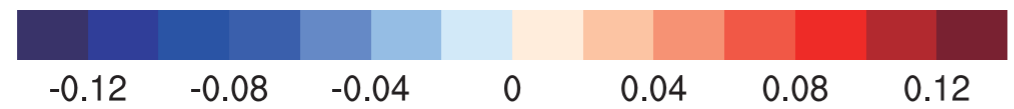
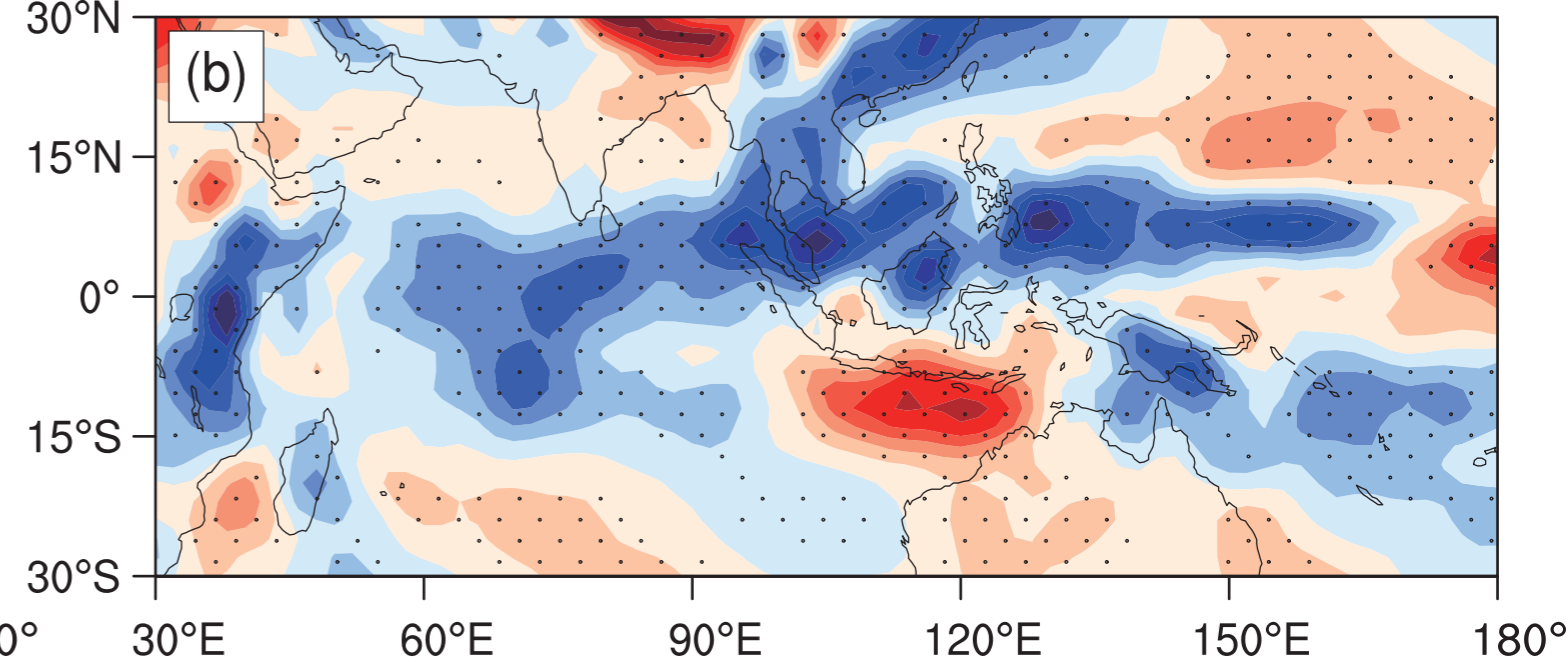
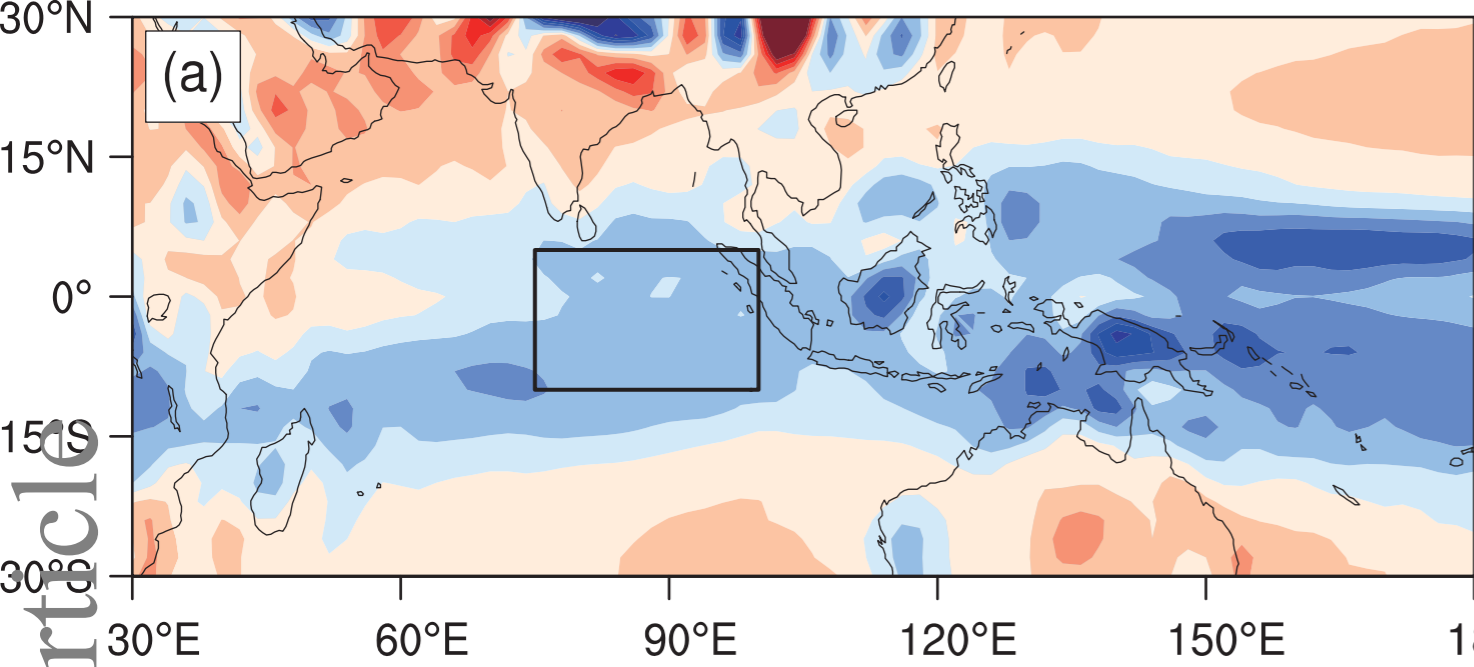
1980

2010

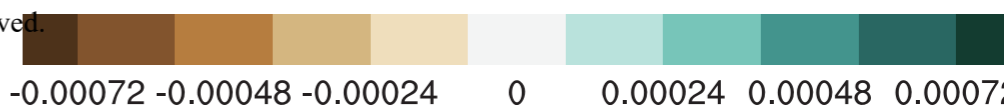
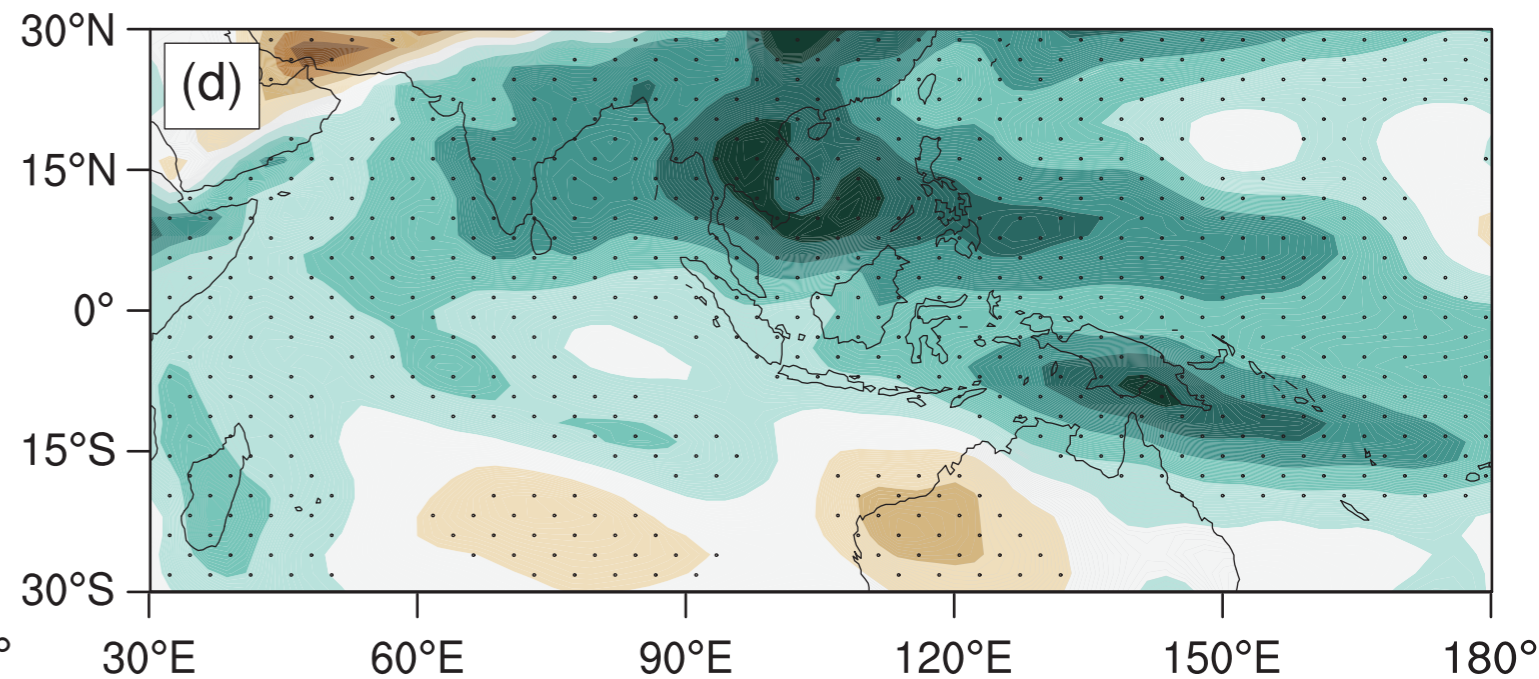
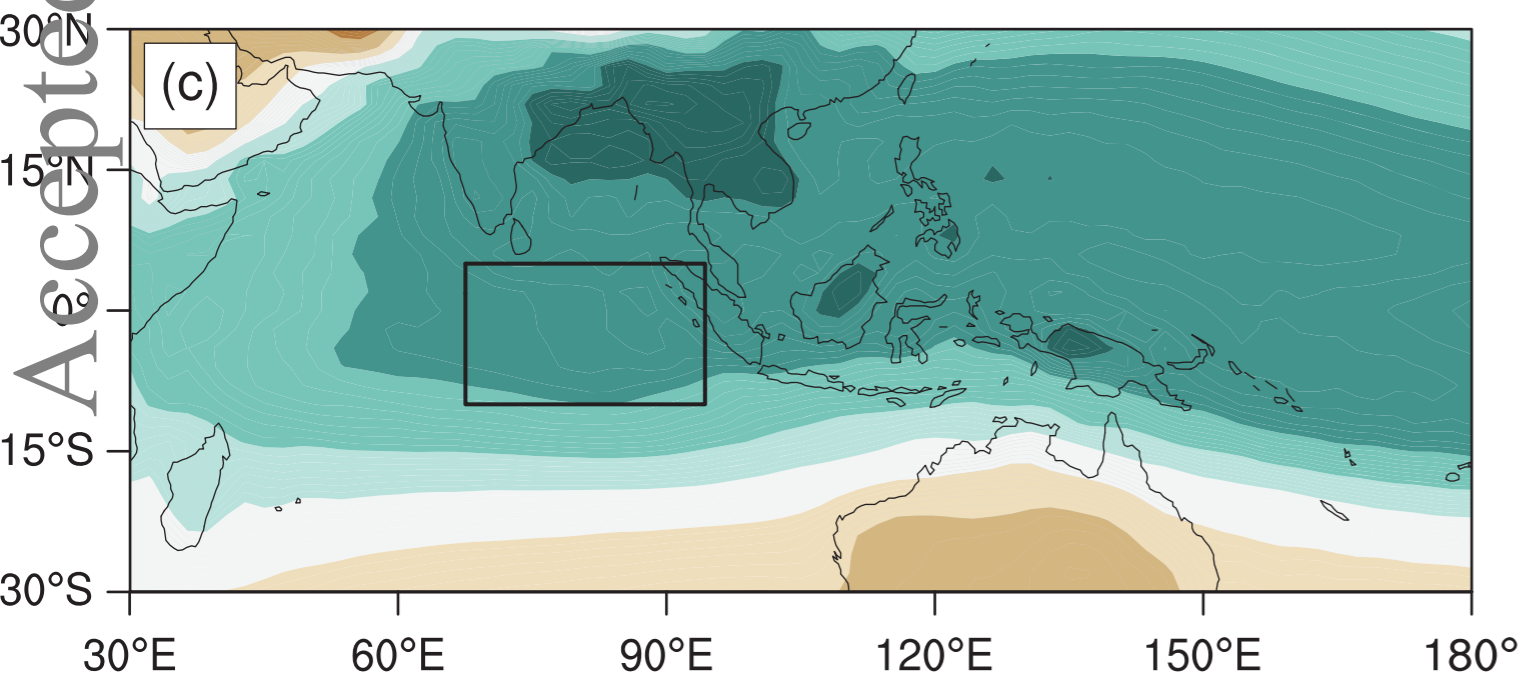
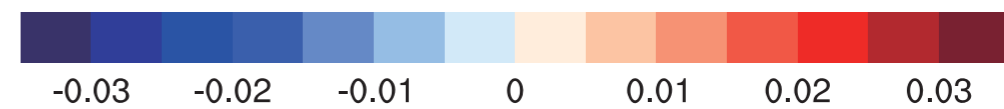
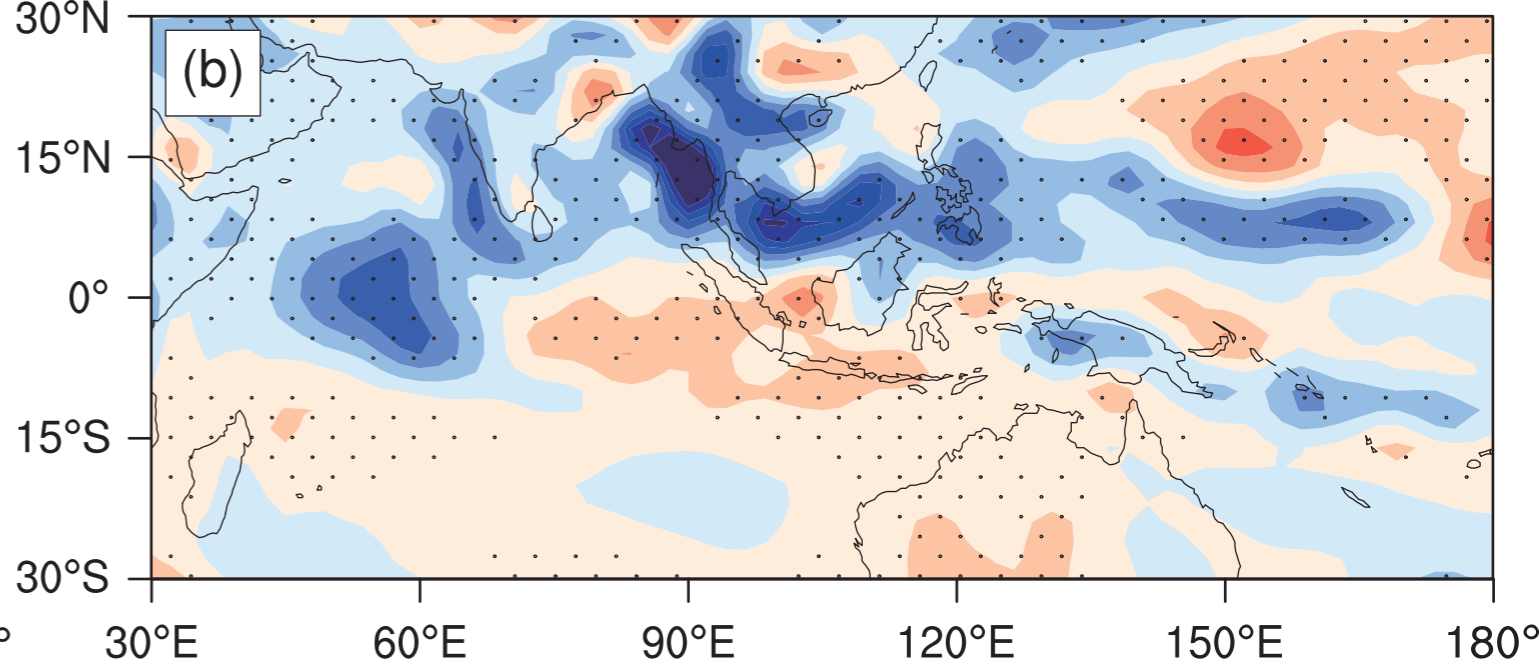
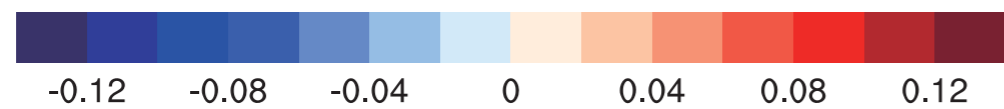
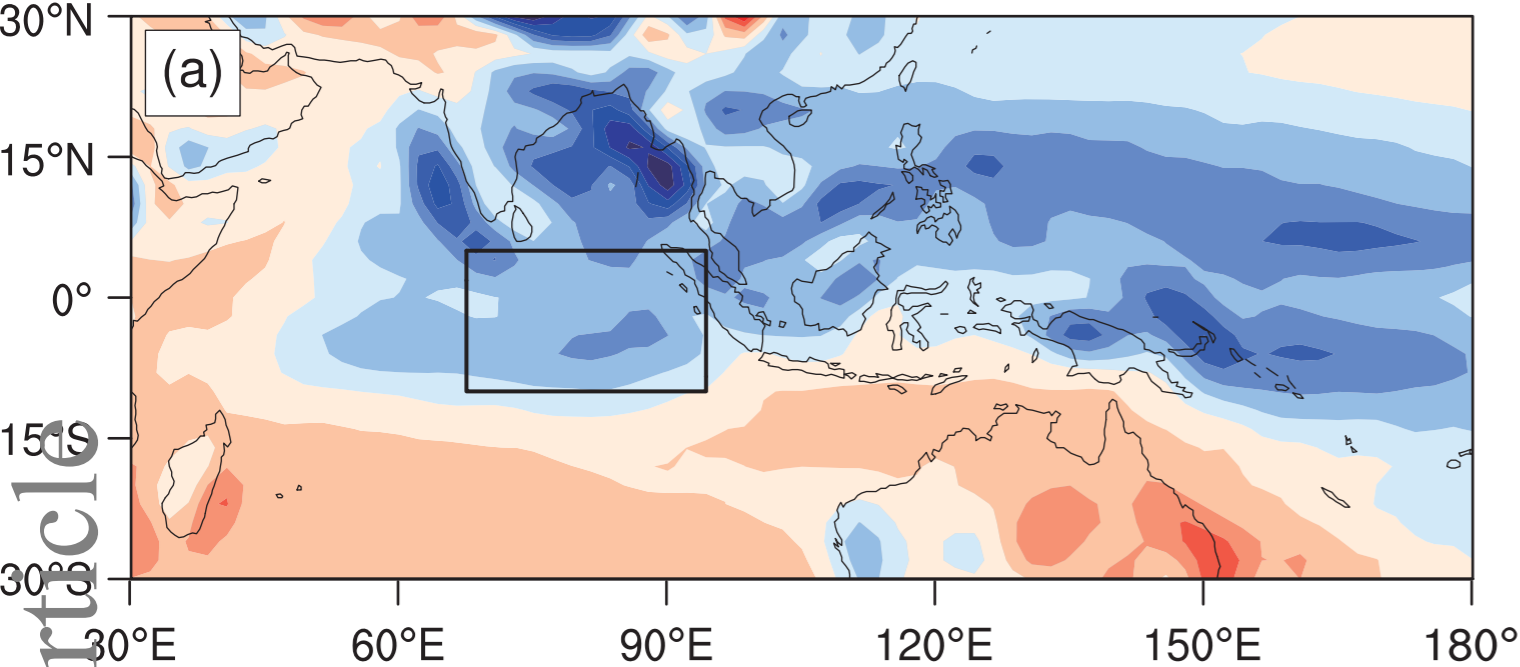


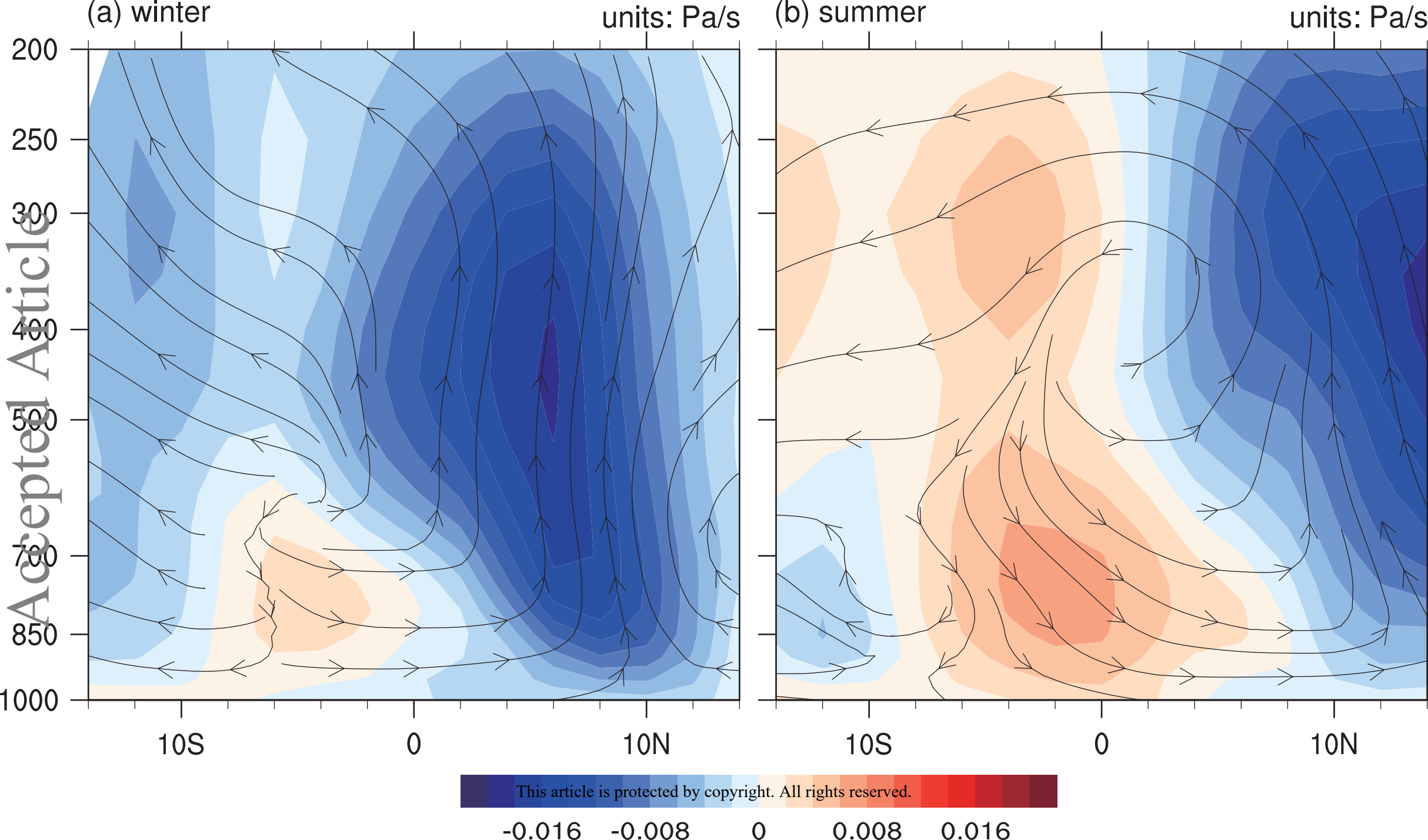


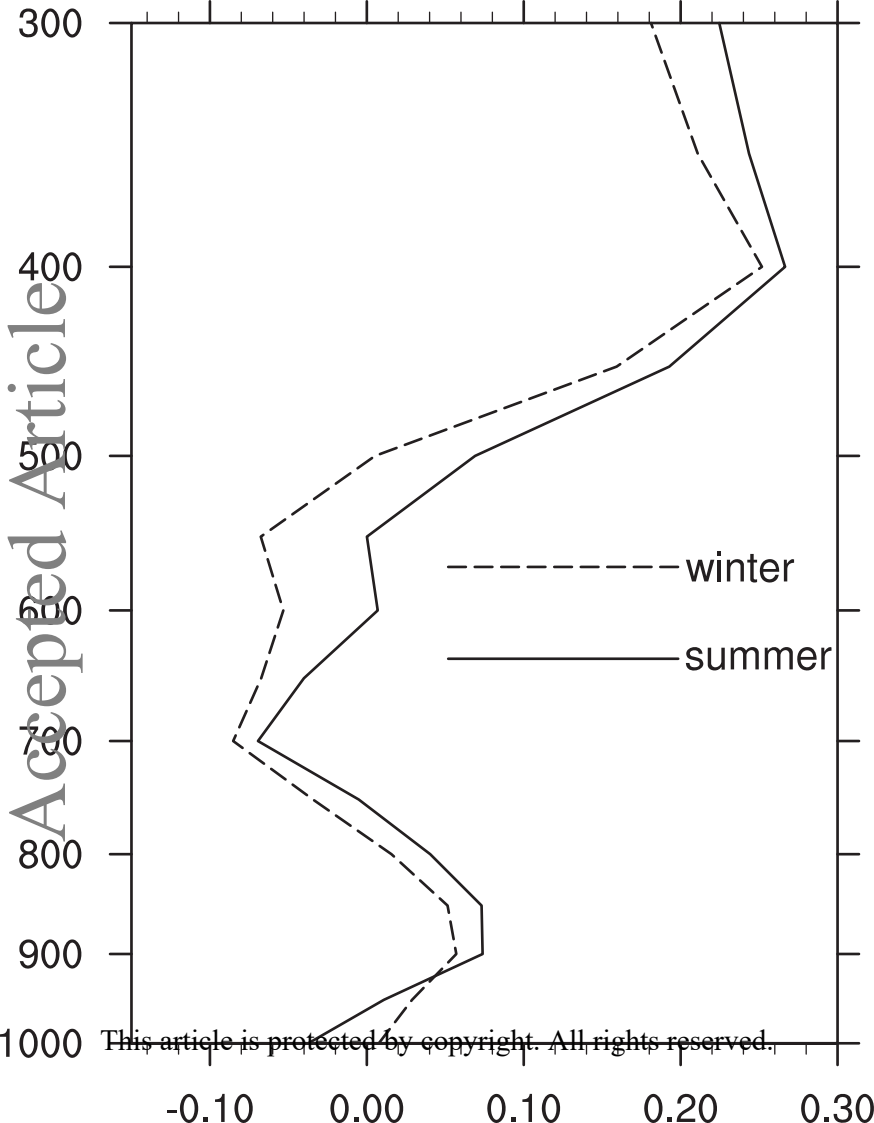
This article is protected by copyright. All rights reserved.



Accepted Article







300

400

500

600

700

800

900

1000

Accepted Article

-0.10

0.00

0.10

0.20

0.30

winter

summer

This article is protected by copyright. All rights reserved.

Accepted Article

